

Surface-based imaging methods for high-resolution functional magnetic resonance imaging

David Ress¹, Sankari Dhandapani¹, Sucharit Katyal¹, Clint Greene¹, Chandra Bajaj²

University of Texas at Austin

¹Imaging Research Center, 3925B West Braker Lane, Austin TX, 78757 USA
ress@mail.utexas.edu

²Center for Computational Visualization, 201 E 24th Street, Austin TX, 78712 USA

Abstract. Functional magnetic resonance imaging (fMRI) has become an exceedingly popular technique for studies of human brain activity. Typically, fMRI is performed with >3 -mm sampling, so that the imaging data can be regarded as two-dimensional samples that roughly average through the typically 1.5–4-mm thickness of cerebral cortex. The use of higher spatial resolutions, <1.5 -mm sampling, complicates the use of fMRI, as one must now consider activity variations within the depth of the brain. We present a set of surface-based methods to exploit the use of high-resolution fMRI for depth analysis. These methods utilize white-matter segmentations coupled with deformable-surface algorithms to create a smooth surface representation at the gray-white interface. These surfaces provide vertex positions and surface normals, vector references for depth calculations. That information enables averaging schemes that can increase contrast-to-noise ratio, as well as permitting the direct analysis of depth profiles of functional activity in the human brain.

Keywords: MRI, fMRI, neuroimaging, brain, laminae

1 Introduction

The human brain is a complex structure that exhibits neural activity on multiple spatial scales. The majority of human brain imaging research focuses on the laminated structure of the cerebral cortex gray matter. Cortical gray matter has a stereotypical 6-layer laminar structure that forms a sheet of tissue 1.5–4-mm thick upon the white matter [2, 4, 11]. The spatial structure of neural activity within cortex can be inferred from its hemodynamic correlates using functional magnetic resonance imaging (fMRI) with blood oxygen-level dependent contrast [10]. High-resolution fMRI can also be used to probe other laminated brain structures such as the superior colliculus and lateral geniculate nucleus [13, 14].

At standard spatial sampling, e.g., 3-mm, activity within cortical gray matter is not resolved. Moreover, these resolutions engender blurring of activity across sulcal boundaries. Because the convoluted shape of the brain brings regions with highly disparate functions into close proximity within the sulci, this kind of blurring can

greatly diminish spatial localization. High resolution is also advantageous because it reduces contamination of cortical activity with noisy and mislocalized activity produced in superficial vascular regions adjacent to cortex. Thus high-resolution fMRI can enhance localization and signal quality for reasons that go beyond the measure of smaller sampling intervals.

In MRI, thermal signal-to-noise ratio varies linearly with voxel volume, so that high-resolution imaging must typically operate in a higher-noise regime for individual images. For example, a typical single T_2^* -weighted functional image with 3-mm sampling will typically have a signal-to-noise ratio (SNR) ~ 250 on a 3T MRI scanner, while at 1-mm-sampling the same image would yield an SNR < 10 . Although there are a variety of methods available to improve the SNR, some measure of appropriate spatial averaging is generally essential.

To deal with these issues, our high-resolution methods generally seek to reconstruct the sampled signals into a very high-resolution (0.6- or 0.7-mm sampling) co-aligned reference anatomy that is segmented to precisely delineate the location of the active brain tissue (e.g., cortical gray matter). Analysis can then be restricted only to those spatial regions within cortex where we expect the best localization and signal quality. A smooth surface is constructed at the inner boundary of the gray matter, where it meets the white matter. The vector reference provided by this surface can then be utilized in two ways: depth averaging to improve the quality of high-resolution surface topography measurements, and to resolve depth variations of cortical activity within a particular portion of the brain.

We illustrate our methods in two portions of the brain: superior colliculus (SC), a small structure in the brainstem with critical functions in eye movements and orientation of attention, and in early visual cortex, the part of cerebral cortex most immediately involved in vision.

2 Methods

2.1 High-resolution structural imaging, segmentation, and surface generation

Imaging was performed on human subjects using a 3-Tesla scanner (General Electric Signa Excite HD) using the product 8-channel head coil. Informed consent was obtained from all subjects based on a protocol approved by the appropriate Institutional Review Board. They were acquired using a three-dimensional (3D), inversion-prepared, radiofrequency-spoiled GRASS (SPGR) sequence (minimum TE and TR, inversion time = 450 ms, 15° flip angle, 2 excitations, ~ 28 -min duration). MRI parameters were chosen so that the structural reference volumes were T_1 -weighted with excellent gray-white contrast. We used an isometric voxel size of 0.6 or 0.7 mm so that the reference volumes would precisely delineate brain tissue boundaries.

Term	Meaning
GRASS	Gradient-recalled acquisition in the steady state. A common technique for creating MRI images.
T_1	Longitudinal relaxation time. The time constant for the recovery of longitudinal magnetization after excitation
T_2^*	Apparent transverse relaxation time. Lifetime of the transverse signal following excitation.
TE	Echo time: the delay between the excitation in image acquisition in MRI.
TR	Repetition time: the interval between excitation of the same tissue during MRI.
FSL	A package of neuroimaging data analysis tools created at Oxford University.
ITK-SNAP	An image processing package developed for the segmentation and rendering of brain image volumes.
FAST	Volume segmentation software based on k-means clustering.
Eccentricity	The radial coordinate from gaze center in visual space; usually measured in degrees.
Polar angle	The angular coordinate in visual space, also measured in degrees.

Table: neuroimaging nomenclature used in this article.

Because all structural image volumes were obtained using surface coil arrays, they exhibited substantial spatial inhomogeneity on several scales. Therefore, volumes were preprocessed using a custom-made software application written in Matlab (MathWorks, Natick, MA). An expert user scanned through the image volume, using a graphical user interface to identify a number of points in the white matter near the gray-white interface on each slice. Intensity values in white matter were then averaged in a $3 \times 3 \times 3$ neighborhood around each point, and these irregularly spaced samples were gridded onto a regular array. Points outside the hull of sampled points were filled in using nearest-neighbor extrapolation. Estimates of noise were also obtained at the sampled points, and this was combined with the interpolated white-matter intensities to create a robust normalization mask that was applied to the brain volume. We then utilized the Brain Extraction Tool (BET) provided in the FSL package [15] to remove superficial non-brain tissue from the volume.

In SC, we segmented the tissue of the midbrain, brainstem, and portions of the thalamus using a combination of automatic and manual methods provided by the ITK-SNAP application [17]. Because the superficial surface of SC exhibits a strong contrast boundary with the surrounding cerebrospinal fluid (CSF), this segmentation was straightforward.

Segmentation of visual-cortex white matter was considerably more difficult. We began by applying the FAST tool in FSL to provide an approximate segmentation [15]. However, some regions exhibited residual inhomogeneity and/or low gray-white contrast-to-noise ratio, and therefore were not accurately segmented. For these regions extensive manual adjustment was necessary to achieve a satisfactory result.

The CSF-tissue interface of the SC and the gray-white interface in visual cortex were interpolated from the corresponding segmentation using isodensity surface rendering. This initial surface was corrupted by aliasing artifacts. To obtain a

smoother representation of the surface and more accurate calculation of its associated surface normal vectors, we used a deformable-surface smoothing algorithm [1, 16]. The deformable surface is based on a curvature-driven geometric evolution, which yields a family of smooth closed immersed orientable surfaces, $\{M(t): t \geq 0\}$ in \mathfrak{R}^3 , according to the solution of the geometric flow,

$$\frac{\partial p}{\partial t} = N(p)V_n(k_1, k_2, p) \quad (1)$$

with $M_0 = M(0)$ defining the initial surface. Here $p(t)$ is a surface point on the $M(t)$, $V_n(k_1, k_2, p)$ denotes the normal velocity of $M(t)$ based on the principal curvatures, $k_{1,2}$ of $M(t)$, and $N(p)$ is the unit normal of $M(t)$ at $p(t)$.

There are basically two classes of solution approaches for spatial discretization of geometric flow equations (1). One approach is based on the use of finite elements (e.g., [1]) and the other on use of finite differences (e.g., [16]). The spatial discretization approach we adopt here is based on finite divided differences obtained by use of discretized differential operators (such as the Laplace-Beltrami) over simplicial (triangulated) surfaces [3]. Discretization for higher order differential operators is defined recursively from the discrete Laplace-Beltrami (see [16] for details). The time discretization of the flow equation (1) is achieved by use of a semi-implicit Euler scheme. Finally, the resulting sparse linear system is solved using an iterative Krylov subspace solver, such as GMRES [12].

In SC, satisfactory results required three iterations of the algorithm; cortex required 6 iterations. We evaluated the accuracy of the refined surfaces by calculating nearest-neighbor distances between their vertices and the vertices of the original surfaces; mean distances were typically <0.3 voxel units, and rarely >0.7 voxels (Fig. 1). These surfaces provided a means to visualize the functional data, as well as vertices and normal vectors used as a reference for the laminar calculations described below. We also approximated the Gaussian curvature of the surface at each vertex as:

$$C = \frac{R}{|R| + \sqrt{A}/4} \quad (2)$$

where R is the signed distance between each vertex and the best-fit plane containing its connected neighbors, and A is the area of all the triangles featuring that vertex. We used this metric as an intensity overlay on our surfaces: positive curvature marking protruding features (e.g., cortical gyri) appear at a light intensity and negative curvature marking intrusive features (e.g., cortical sulci) appear as a dark intensity. This binary curvature overlay improves the 3D perception of the surface, and also provides a useful indicator of aliasing artifacts.

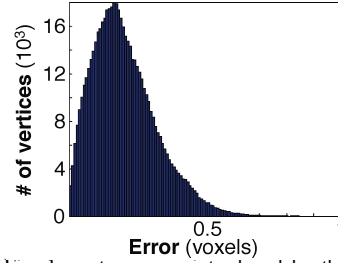


Fig. 1: vertex errors introduced by the mesh refinement procedure.

2.2 Functional MRI

We illustrate our methods with functional image sets obtained in two brain regions: SC and early visual cortex. In SC, we again used the product head coil array to obtain time series of images on eight 1.2-mm-thick quasi-axial slices (170-mm field-of-view [FOV]) with the prescription oriented roughly perpendicular to the local neuraxis. In visual cortex we used a custom-made 7-channel surface coil array packaged in a flexible former so that it could be closely positioned against the subject's head. This array produces images with an SNR advantage of 2–4 over the product coil, depending upon depth. By choosing a tangential, quasi-coronal orientation at the back of the head, we could limit our FOV to 90–100 mm. Use of the surface coil and smaller FOV enabled imaging with 0.7 or 0.8-mm sampling. We obtained 8–12 such slices oriented approximately perpendicular to the calcarine sulcus

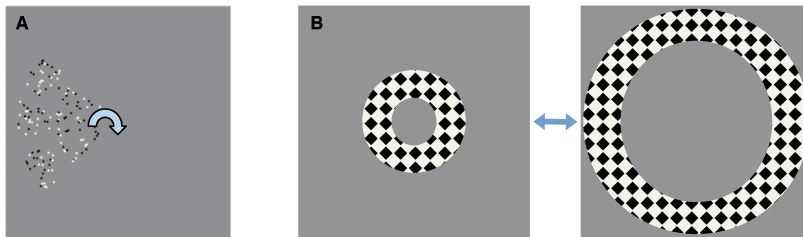


Fig. 2. Visual stimulus configurations: A) rotating wedge of moving dots to map polar angle visual-field variation in SC; B) alternating annuli to stimulate portions of early visual cortex.

The SC experiments used travelling-wave techniques to map its retinotopic coordinate representation of the visual field. Stimulus was a 90° wedge of moving dots that rotated slowly (24-s period) around a fixation mark (Fig. 2A). The entire stimulus rotated 9.5 times around fixation with a period of 24 seconds while subjects maintained fixation. Many MRI runs (14–18) were obtained using this stimulus presentation in each 2-hour-long scanning session.

The visual cortex experiments used a stimulus designed to activate substantial portions of posterior early visual cortex. Subjects viewed a high-contrast grating within an annular mask (Fig. 2B) that alternated (18-s period) in position from small eccentricity (0.5–1.25°) to larger eccentricity (1.5–2.5°). This alternation was repeated 10.5 times to create ~3-min duration runs. Typically 8–12 runs were collected for each scanning session.

Functional images were acquired during the stimulus presentations. For excitation, we utilized a 6.4-ms windowed-sinc pulse to provide sharp slice-select resolution. For acquisition, we used a three-shot outward-spiral trajectory [5, 6] in all imaging. In SC, echo time was 40 ms, while in cortex we used 30 ms because we measured a correspondingly longer T_2^* in SC tissue (~60 ms) than typically observed in cortical gray matter (~45 ms). Acquisition bandwidth was limited to 60 kHz to reduce peak

gradient current that causes unwanted heating on our scanner. We chose $TR = 1$ s, so that a volume was acquired every 3 s.

The multiple shots were combined together after correction by subtracting the initial value and linear trend of the phase. Image reconstruction was done by gridding with a Kaiser-Bessel kernel using 2:1 oversampling. TE was incremented by 2-ms on the first frame to estimate a field map from the first two volumes acquired, and this map was used for linear correction of off-resonance image artifacts [7]. Concomitant field effects arising during the readout gradients were corrected with a time varying phase [5]. Reconstructed images had a SNR of ~ 20 in both experiments.

In all imaging experiments, a set of T_1 -weighted structural images was obtained on the same prescription as the functional data at the end of the session using a 3D SPGR sequence (15° flip angle, 0.7-mm pixels). These images were used to align the functional data to the segmented structural reference volume.

We estimated in-scan motion using a robust scheme [9] applied to a boxcar-smoothed (3–5 temporal frames) version of the fMRI time-series data. Between-scan motion was corrected using the same intensity-based scheme, this time applied to the temporal average intensity of the entire scan. The first scan of the session was used as the reference. After motion correction, the many runs recorded during each session were averaged together to improve SNR.

The intensity of the averaged data was spatially normalized to reduce the effects of coil inhomogeneity. The normalization used a homomorphic method, that is, dividing by a low-pass filtered version of the temporally averaged volume image intensities with an additive robust correction for estimated noise. A sinusoid at the stimulus repetition frequency was then fit to the normalized time series at each voxel, and from this fit we derived volume maps of response amplitude, coherence, and phase. The coherence value is equivalent to the correlation coefficient of the time-series data with its best-fit sinusoid. Functional data were then aligned and resampled to the reference volume [9].

2.3 Laminar analysis

A distance map was calculated between the tissue voxels and the vertices of the associated surface. We used these distances to measure laminar position (i.e., depth, s) in the reference volume. Thus, the functional data (e.g., complex amplitudes) at each volume voxel were now associated with a depth coordinate.

These associations were used to calculate laminar profiles of functional activity within small disk-shaped regions (1.6–2.4-mm-diam) regions across the surface of the activated portion of the brain. Within these regions, we obtained the complex amplitude as a function of depth for all runs averaged together [11]. A boxcar-smoothing kernel was convolved with the average complex amplitude data as a function of depth; the magnitude of this convolution was the laminar profile.

For each profile, we define the functional thickness, s_f , from spatial moments of the laminar amplitude profile, $A(s)$:

$$\hat{A} = \int_{s_{\min}}^{s_{\max}} A(s) ds \quad (3)$$

$$\bar{s} = \frac{1}{\bar{A}} \int_{s_{\min}}^{s_{\max}} s A(s) ds \quad (4)$$

$$s_f = 2 \left[\frac{1}{\bar{A}} \int_{s_{\min}}^{s_{\max}} (s - \bar{s})^2 A(s) ds \right]^{1/2} \quad (5)$$

where s_{\min} and s_{\max} are the boundaries of the laminar segmentation. Typically, we chose an interval of $[-2, 5]$ mm. Note that the subtraction of the depth centroid, \bar{s} , makes s_f less sensitive to alignment errors. Thus, we associate the functional thickness with every vertex on the surface, enabling the display of functional thickness as a colormap overlay on the rendered surface.

For the SC data, we also used the laminar segmentation process to enable depth averaging that improves the quality of data. For each point on the surface, the associated disk-shaped segmentation was used to average the complex amplitude data over a particular depth range. As part of our mapping process, we generally extracted the phase values from the mean complex amplitudes, and displayed these at the corresponding vertex of the surface. Coherence values were specified as the maximum value over the depth range.

3 Results

3.1 High-resolution structural imaging, segmentation, and surface generation

We present two examples of the high-resolution MRI data. In SC, the images clearly delineate the strong contrast boundary at its superficial dorsal surface. The segmentation, which includes nearby portions of midbrain, thalamus, and brainstem, is shown by a blue overlay (Fig. 3A). The boundary of this segmentation was rendered as a surface, upon which a binary curvature map is overlaid, with a light

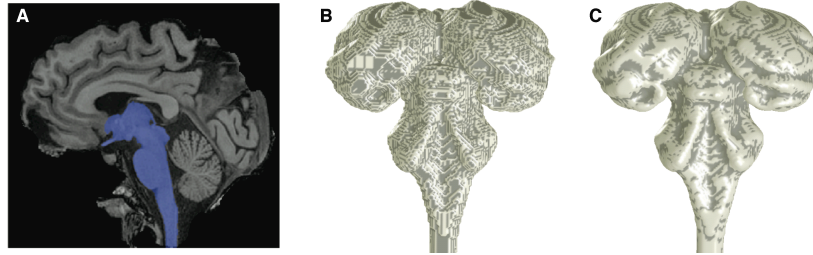


Fig. 3. Human superior colliculus: A) segmentation, including adjacent midbrain, thalamus, and brainstem structures; B) initial surface; C) refined surface.

shade indicating positive curvature, and a dark shade indicates negative curvature. The fine-scale structure evident in the curvature map is caused by aliasing artifacts in the initial surface (Fig. 3B). After application of the deformable surface algorithm [16], the high spatial frequency curvature artifacts largely disappear, leaving only the actual gross features of the anatomy (Fig. 3C).

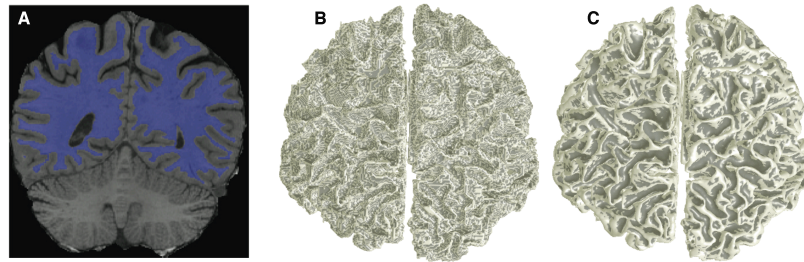


Fig. 4. Human cerebral cortex: A) segmentation; B) initial surface; C) refined surface.

For visual cortex, we segment the entirety of the cerebral hemispheres, but pay particular attention to manual adjustment of the initial segmentation in the occipital lobe (Fig. 4A). The initial isodensity surface once again shows extensive aliasing artifacts, visible as the fine stipple in the curvature overlay (Fig. 4B), that are again greatly reduced by application of the deformable surface algorithm [16] (Fig. 4C).

3.2 Functional MRI

For the SC visual field mapping experiments, we are principally interested in the phase of the sinusoidal fits. Typical data from one inplane slice, thresholded at a coherence of 0.3, is shown as a color overlay upon their corresponding inplane anatomy images in Fig. 5. The color wheel shows how the phase angle is related to visual field angle. Note the phase progression across the superficial surface of the SC, as well as in posterior visual cortex. This data is then transformed into the reference volume for that subject, so that it can be mapped onto the associated surface representations. The visual cortex data, where we are interested in the complex sinusoidal fit amplitudes, are similarly transformed from the inplane coordinates into the reference volume for that subject.

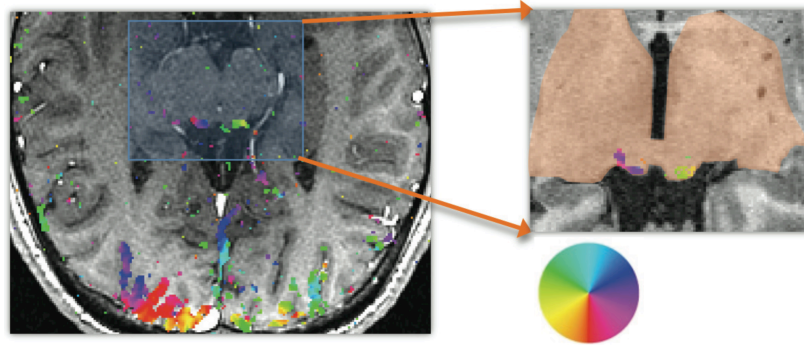


Fig. 5. Functional MRI phase data as color overlay on inplane structural MRI (*left*) and transformed into reference volume (*right*). Color wheel shows relationship to visual field angle.

3.3 Laminar analysis

The SC data was analyzed in two ways. First we performed the disk-like segmentation described above, averaged the complex amplitudes through a depth range of 0–1.8 mm, and then extracted the phase. This procedure produces high-quality visual field maps (Fig. 6A), despite fairly low response magnitudes (~0.3% modulation with respect to the mean intensities). Phase maps prepared without the laminar segmentation and depth averaging are much noisier, as can be quantified by calculating session-to-session correlations. We also used our depth-mapping techniques to form laminar profiles of the SC activity in three regions-of-interest (ROIs) that span the surface of the SC from lateral to medial (Fig. 6B). These profiles show that activity is evident principally in the superficial 2 mm of the SC tissue, which is known to correspond to a preponderance of visually responsive neurons. The data also show significantly thinner profiles for the medial ROI than for the lateral and central ROIs, which is consistent with the known anatomy of human SC.

The visual cortex data was analyzed to calculate the functional thickness metric, which was visualized as a color overlay upon surface renderings of the posterior portions of the left hemisphere of a brain (Fig. 7A). This data can then be compared to structural measurements of the actual gray-matter thickness visualized in the same fashion (Fig. 7B). The functional and structural thickness data are strongly and significantly correlated. Both show the characteristic pattern of gray matter thickness: thicker on crowns of the gyri and thinner in depths of the sulci.

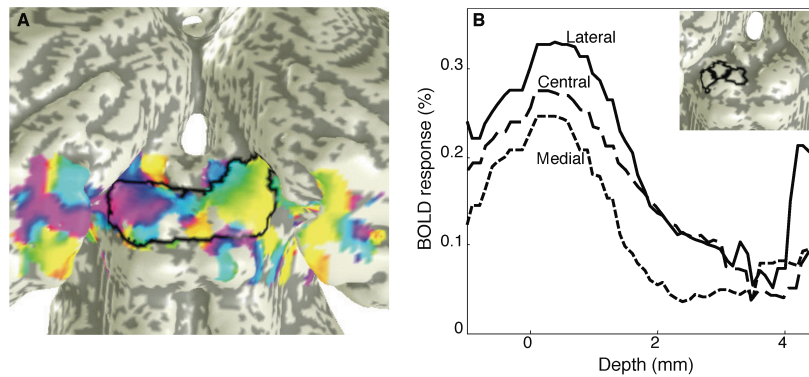


Fig. 6. Analyzed data from human SC: A) Visual field maps on the surface of the SC, with quality enhanced by depth averaging. Boundaries of SC are indicated by the black outline. B) profiles of SC activity as a function of depth within the tissue for three ROIs (*lateral: solid, central: long dashes, medial: short dashes*). Inset shows the locations of the depth-profile ROIs: lateral, central and medial (*left to right*).

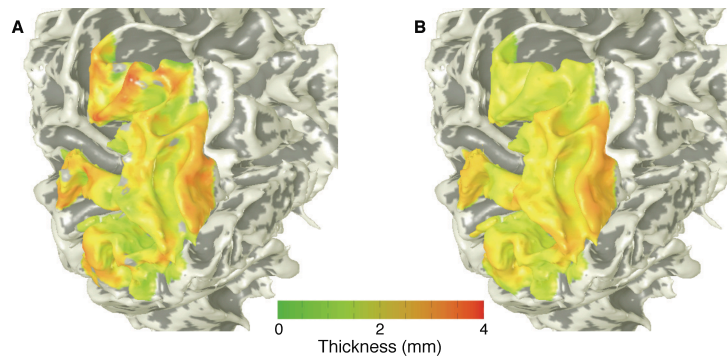


Fig. 7. Data from human visual cortex: A) functional thickness; B) structural thickness.

4 Discussion

We have presented a set of surface-based methods for the analysis of high-resolution fMRI data. The analysis requires the acquisition of a high-resolution structural volume that is segmented to obtain a relevant tissue interface. This interface, in turn, is used for the generation of smooth surface that provides a geometric reference, in

the form of vertices and surface. We make use of this geometry by transforming fMRI data into the reference volume. Specifically, we can construct depth profiles of the functional activity, or average the data along the surface to improve signal quality and enhance our visualization capabilities.

These procedures can essentially be viewed as a solution to a classic digital reconstruction problem: converting data sampled in one coordinate system to another. Specifically, here we take regularly sampled MRI data, and resample them into the natural coordinates of the segmented tissue boundary. This procedure is particularly useful for fMRI data, which can be subject to artifacts and mislocalization associated with superficial vascular artifacts [8, 11]. The surface based methods become particularly attractive at high spatial resolution, where the Cartesian-space sampled data begin to resolve brain function in 3D, including both the transverse extent of the brain surface as well as its laminar depth.

Acknowledgments. We thank the VISTA lab at Stanford University, particularly Bob Dougherty and Brian Wandell, for their assistance in developing some of the visualization tools and fMRI analysis methods described here. We are also grateful to Gary Glover for providing the MRI spiral-acquisition pulse sequence. Research for CB was supported in part by NIH grants R01EB00487, R01GM074258, and R01GM07308.

References

1. Bajaj, C.L., Xu, G.: Anisotropic diffusion of surfaces and functions on surfaces. *ACM Trans. Graph.* **22** (2003) 4-32
2. Braitenberg, V., Schutz, A.: *Anatomy of cortex*. Springer-Verlag, Berlin (1991)
3. Desbrun, M., Meyer, M., Schröder, P., Barr, A.: Discrete Differential-Geometry Operator for Triangulated 2-manifolds. *Proceedings of Visual Mathematics'02*, Berlin, Germany (2002)
4. Fischl, B., Dale, A.M.: Measuring the thickness of the human cerebral cortex from magnetic resonance images. *Proc Natl Acad Sci U S A* **97** (2000) 11050-11055
5. Glover, G.H.: Simple analytic spiral K-space algorithm. *Magn Reson Med* **42** (1999) 412-415
6. Glover, G.H., Lai, S.: Self-navigated spiral fMRI: interleaved versus single-shot. *Magn Reson Med* **39** (1998) 361-368
7. Glover, G.H., Law, C.S.: Spiral-in/out BOLD fMRI for increased SNR and reduced susceptibility artifacts. *Magn Reson Med* **46** (2001) 515-522
8. Moon, C.H., Fukuda, M., Park, S.H., Kim, S.G.: Neural interpretation of blood oxygenation level-dependent fMRI maps at submillimeter columnar resolution. *J Neurosci* **27** (2007) 6892-6902
9. Nestares, O., Heeger, D.J.: Robust multiresolution alignment of MRI brain volumes. *Magn Reson Med* **43** (2000) 705-715

10. Ogawa, S., Menon, R.S., Kim, S.G., Ugurbil, K.: On the characteristics of functional magnetic resonance imaging of the brain. *Annu Rev Biophys Biomol Struct* **27** (1998) 447-474
11. Ress, D., Glover, G.H., Liu, J., Wandell, B.: Laminar profiles of functional activity in the human brain. *NeuroImage* **34** (2007) 74-84
12. Saad, Y.: *Iterative Methods for Sparse Linear Systems*. Society for Industrial and Applied Mathematics, Chicago (2002)
13. Schneider, K.A., Kastner, S.: Visual responses of the human superior colliculus: a high-resolution functional magnetic resonance imaging study. *J Neurophysiol* **94** (2005) 2491-2503
14. Schneider, K.A., Richter, M.C., Kastner, S.: Retinotopic organization and functional subdivisions of the human lateral geniculate nucleus: a high-resolution functional magnetic resonance imaging study. *J Neurosci* **24** (2004) 8975-8985
15. Smith, S.M., Jenkinson, M., Woolrich, M.W., Beckmann, C.F., Behrens, T.E., Johansen-Berg, H., Bannister, P.R., De Luca, M., Drobnjak, I., Flitney, D.E., Niazy, R.K., Saunders, J., Vickers, J., Zhang, Y., De Stefano, N., Brady, J.M., Matthews, P.M.: Advances in functional and structural MR image analysis and implementation as FSL. *NeuroImage* **23 Suppl 1** (2004) S208-219
16. Xu, G., Pan, Q., Bajaj, C.L.: Discrete Surface Modeling Using Partial Differential Equations. *Computer Aided Geometric Design* **23/2** (2006) 125-145
17. Yushkevich, P.A., Piven, J., Hazlett, H.C., Smith, R.G., Ho, S., Gee, J.C., Gerig, G.: User-guided 3D active contour segmentation of anatomical structures: significantly improved efficiency and reliability. *NeuroImage* **31** (2006) 1116-1128